Acta Crystallographica Section D
Biological Crystallography
ISSN 0907-4449

Crystallization of mitochondrial respiratory complex II from chicken heart: a membrane-protein complex diffracting to 2.0 Å

Li-shar Huang, Toni M. Borders, John T. Shen, Chung-Jen Wang and Edward A. Berry*

Physical Biosciences Division, Lawrence Berkeley National Laboratory, One Cyclotron Road, Berkeley CA 94720, USA

Correspondence e-mail: eaberry@lbl.gov

Received 2 November 2004
Accepted 4 January 2005

A procedure is presented for preparation of diffraction-quality crystals of a vertebrate mitochondrial respiratory complex II. The crystals have the potential to diffract to at least 2.0 Å with optimization of post-crystal-growth treatment and cryoprotection. This should allow determination of the structure of this important and medically relevant membrane-protein complex at near-atomic resolution and provide great detail of the mode of binding of substrates and inhibitors at the two substrate-binding sites.

1. Introduction

The mitochondrial respiratory chain oxidizes reduced substrates using molecular oxygen and couples the resulting energy release to translocation of protons across the mitochondrial inner membrane. This results in an energized state residing in the transmembrane gradient of electrochemical potential of the proton ($\Delta\mu_{H^+}$) that is used to drive various endergonic processes including synthesis of ATP by the F_1F_o ATP synthase. In the 1960s, scientists working on resolution and reconstitution of the mitochondrial respiratory chain were able to fractionate the chain into four 'complexes' (Green *et al.*, 1965) containing NADH:ubiquinone oxidoreductase (complex I), succinate:ubiquinone oxidoreductase (complex II), ubiquinol:cytochrome *c* oxidoreductase (complex III) and cytochrome oxidase (complex IV) activities. The F_1F_o ATP synthase is sometimes referred to as 'complex V'. Detergent was required for the fractionation, as all four complexes are transmembraneous integral membrane-protein assemblies. Although there is some evidence for higher level organization into 'supercomplexes' (Stroh *et al.*, 2004), it appears that the four 'complexes' do in fact represent organizational units and individual (multi-subunit) enzymes. The number of non-identical subunits ranges from around 50 in the case of complex I to only four for complex II, with mitochondrial complex III having 10–11 and complex IV 13 subunits.

Complex II (Ackrell, 2000; Cecchini, 2003; Hagerhall, 1997; Lancaster, 2003) is unique in being a member of the Krebs TCA cycle as well as the respiratory chain. In addition to detergent-solubilized preparations of complex II, a soluble preparation of 'succinate dehydrogenase' could be prepared by treating mitochondrial membranes with chaotropes, alkaline pH and/or organic solvent (Bernath *et al.*, 1956; Davis & Hatefi, 1971*b*; Wang *et al.*, 1956). The kinetics and regulatory properties of both soluble and 'particulate' succinate dehydrogenase have been studied extensively (Singer *et al.*, 1973). The enzyme has an activated and a 'deactivated' state which interconvert slowly with a high activation energy. The equilibrium between the two states is affected by substrates and

© 2005 International Union of Crystallography
Printed in Denmark – all rights reserved

competitive inhibitors, phosphate, some nucleotides and the redox state of the mitochondrial ubiquinone pool. The significance of these regulatory mechanisms is unclear, however, as the amount of activity in the mitochondrion is so high that even in the 'deactivated' state SDH seems not to be rate-limiting (Singer *et al.*, 1973). This suggests that complex II may be involved in regulating some other cellular process.

A number of cellular defects and myopathies are known to result from defects in respiratory-chain enzymes. These are often associated with accumulation of mitochondrial DNA damaged with aging as a result of exposure to radicals produced by the oxidative machinery. Complex II is exempt from such problems, as all four subunits are encoded on cytoplasmic genes in higher eukaryotes. Nonetheless, complex II is involved in some hereditary cytopathies (Ackrell, 2002).

A loss of complex II (together with complexes III and IV) in neural tissues is observed in Huntington's disease. That this is directly involved in the disease and not simply a side effect is indicated by the fact that inhibition or genetic manipulation of complex II leads to Huntington-like symptoms (Beal *et al.*, 1993). More recently, a role has been proposed for complex II in the induction of apoptosis (Albayrak *et al.*, 2003). Perhaps related to this, complex II subunits have been identified as tumor suppressors (Baysal *et al.*, 2000; McDonnell *et al.*, 2004; Niemann & Muller, 2000). Complex II is also a target or potential target for agrochemical and clinical drugs, for example the complex II inhibitor carboxin, which is commercially available as 'Vitavax', and the fungicide flutolanil, which has recently been shown to act on complex II (Ito *et al.*, 2004).

Complex II consists of four non-identical subunits. The site where succinate is oxidized resides in a 68 kDa flavoprotein (FP; chain *A*), which together with a 28 kDa subunit containing three iron–sulfur clusters (IP; chain *B*) makes up the soluble succinate dehydrogenase. The other two subunits (*C* and *D*) are small hydrophobic 'anchor' peptides, 16 and 11 kDa in the case of vertebrate complex II. It was recognized early on by some investigators (Davis & Hatefi, 1971*a*) that complex II included a *b*-type cytochrome, although others suspected the cytochrome was a contaminant from complex III (Wikstrom, 1973; Yu & Yu, 1980). Later, homologous bacterial proteins were discovered with zero, one or two hemes per flavin (reviewed in Hagerhall, 1997; Lancaster, 2001). It is now agreed that the small anchor subunits of the mitochondrial enzyme contain one heme and the site where ubiquinone is reduced.

The α-proteobacteria have a respiratory chain that is quite similar to that of mitochondria. Of these organisms, complex II subunits *A*, *B*, *C* and *D* have sequence identity with the human enzyme as high as 64, 71, 29 and 36% (*Rhodospirillum rubrum*), respectively. The more distantly related γ-proteobacterium *Escherichia coli* has two homologs of complex II (Cecchini *et al.*, 2002). Of these, the more closely related SQR functions like the mitochondrial enzyme to oxidize succinate in aerobic respiration and has a sequence identity with the human enzyme of around 55% for both large subunits. The other *E. coli* complex, FRD, is expressed anaerobically and functions to reduce fumarate as the terminal acceptor of an anaerobic respiratory chain; it shows less sequence homology.

Low- to medium-resolution structures of both *E. coli* complexes have been determined (Iverson *et al.*, 2002; Yankovskaya *et al.*, 2003). However, no experimentally determined structure is available for vertebrate complex II, or for any mitochondrial complex II for that matter. The available structure of yeast complex II (PDB code 1pb4; Oyedotun & Lemire, 2004) was derived by homology modeling based on bacterial complexes and we feel it serves as much to emphasize the need for a mitochondrial structure as to fill that need.

We report here a reproducible procedure for purification and crystallization of complex II from avian heart mitochondria and preliminary cryoprotection conditions that permit diffraction to as high as 2.0 Å. Thanks in part to chicken genome projects at the University of Delaware and the Roslin Institute (Boardman *et al.*, 2002), the entire sequence of all four subunits of chicken complex II are known. Sequence identity between the human and chicken proteins is 91, 90, 72 and 80% for the mature forms of the *A*, *B*, *C* and *D* subunits, respectively. Data sets have been collected with a number of product and inhibitor compounds co-crystallized in order to determine the binding mode of these compounds. The structure has been solved by molecular replacement and is currently being refined against a 2.2 Å data set.

2. Methods

2.1. Purification

2.1.1. Assay. Activity was verified by measuring the rate of DCPIP reduction in the presence of succinate and PMS; however, for routine monitoring of fractions UV–visible spectroscopy and SDS–PAGE were used.

2.1.2. Detergent extraction. Mitochondria were prepared from chicken hearts essentially by the method of Smith (1967) and resuspended in buffer and THESIT detergent ($C_{12}E_N$; PEG 400 dodecyl ether; Fluka #17228) to give final concentrations of 50 m*M* potassium phosphate pH 7.5 (KP_i), 20 g l^{-1} protein and 30 g l^{-1} THESIT. The mixture was homogenized and incubated for 30 min at 277 K before centrifugation.

2.1.3. TSK column. The supernate was diluted with nine volumes of cold water and applied onto a column of DEAE-650S ToyoPearl TSK-gel. The column was washed with 17.5 m*M* KP_i and 1.75 g l^{-1} THESIT and eluted with a gradient of 17.5–50 m*M* KP_i, 1.75–5 g l^{-1} THESIT. Fractions were pooled based on visible spectra.

2.1.4. Hydroxyapatite. The fractions containing complex II were pooled, diluted with 0.43 volumes of cold water to bring the phosphate concentration to 35 m*M* and applied onto Ceramic Hydroxyapatite (Biorad type II, 80 µm). Complex II binds weakly and was collected in the flowthrough and in ten column volumes of washing buffer (35 m*M* KP_i, 3.5 g l^{-1} THESIT).

2.1.5. DEAE-Sepharose. These fractions were pooled and further diluted with one volume of cold water before applying onto a DEAE-Sepharose column (~60 × 2.5 cm). Complex II

binds and remains bound during washing with 17.5 m*M* KP_i, 1.75 g l^{-1} THESIT. It was eluted in a gradient of 17.5–50 m*M* KP_i with 1.75–5.0 g l^{-1} THESIT.

2.1.6. Ammonium sulfate fractionation. Solid ammonium sulfate was added to the pooled fractions to achieve 28% saturation at 277 K and phase-separated detergent/lipids/protein was removed by centrifugation, yielding a gummy floating 'pellet'. The infranate was brought to 40% saturation by addition of further solid ammonium sulfate and centrifuged to yield a crisp friable pellet (if this pellet was gummy, the percentage saturation in the first step was increased to remove more of the 'gum') which dissolved readily in 20 m*M* K MOPS pH 7.2, 100 m*M* NaCl, 0.5 m*M* EDTA, 0.1 g l^{-1} DM (S-300 column buffer). Sufficient buffer was added to ensure that the protein was completely dissolved and the product was then concentrated to 10–15 ml by ultrafiltration on a YM-100 membrane.

2.1.7. Sephacryl S-300. This material was applied onto a 102 × 2.5 cm S-300 column equilibrated with S-300 column buffer. The column was eluted with the same buffer, recycling the effluent back to the top of the column once for greater resolution prior to collecting fractions. This isolates one aggregation state, presumed to be the monomer (see §3).

2.1.8. Density gradient. Further separation of aggregated or dissociated material was achieved by concentrating to ∼5 ml and loading on a glycerol density gradient of 20–40% glycerol in 20 m*M* Tris–HCl pH 7.5, 100 m*M* NaCl, 0.5 m*M* EDTA and 0.5 g l^{-1} dodecyl maltoside. This was centrifuged for 16 h at 45 000 rev min^{-1} in a Beckman Type 70-Ti fixed-angle rotor. The colored band in the lower half of the gradient was collected, leaving some yellowish material in the upper half and a small button of pelleted material.

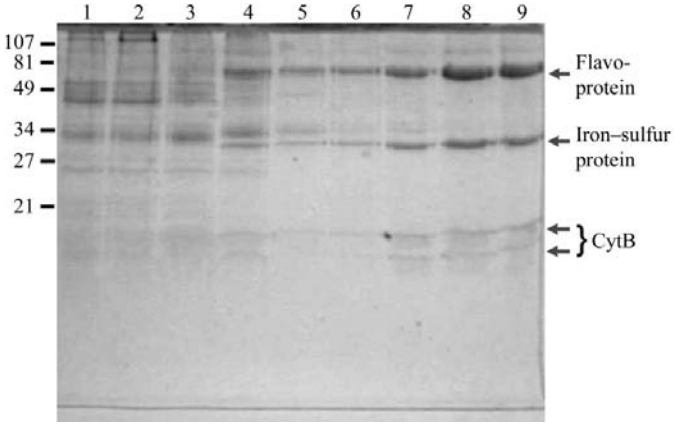

Figure 1
SDS–polyacrylamide gel analysis at different stages during purification. Positions of molecular-weight standards are indicated on the left and the four subunits of complex II are labeled on the right. Lane 1, whole mitochondria. Lane 2, residue from detergent extraction. Lane 3, detergent extract. Lane 4, pooled fractions, TSK column. Lane 5, pooled flowthrough fractions, hydroxyapatite column. Lane 6, pooled fractions from DEAE-Sepharose elution. Lane 7, ammonium sulfate fractionation, 40% saturation pellet. Lane 8, pooled fractions from Sephacryl S-300 column. Lane 9, pooled fractions from glycerol density-gradient centrifugation.

The collected material was concentrated and exchanged into 10 g l^{-1} octyl glucoside in 20 m*M* Tris–HCl pH 7.5, 0.5 m*M* EDTA by repeated concentration in an Amicon/Millipore Centriplus centrifugal ultrafiltration device with a YM-100 membrane, ending with a final concentration of around 0.4–0.8 m*M* (50–100 g l^{-1} protein).

2.2. Crystallization and post-crystallization treatments

2.2.1. Crystallization. Crystallization took place by vapor diffusion in the sitting-drop format. To set up crystallization droplets, 15 µl of concentrated protein in the above buffer was mixed with an equal volume of precipitant containing 0.1 *M* HEPES pH 7.5, 5% 2-propanol, 100 g l^{-1} PEG 3350, 3 m*M* NaN_3 and various additives, for example 1.3 m*M* $MgCl_2$, 1.6 m*M* $MnCl_2$ and 15 ml l^{-1} PEG 400 (final concentrations) in the case of most crystals reported here. These were added from concentrated solutions to avoid excessive dilution. The sitting droplets were equilibrated against reservoirs containing the precipitant alone. The droplets were set up at room temperature and incubated at 277 K.

2.2.2. Co-crystallization. For co-crystallization with tight-binding inhibitors, water-soluble compounds were added in a twofold molar excess from a concentrated stock solution before mixing with precipitants. Alcohol-soluble compounds were added from ethanolic stock solution before the last concentration step in order to avoid excessive alcohol concentrations. Compounds that have been successfully co-crystallized and for which diffraction data (2.2–2.5 Å) have been collected include oxaloacetate, malonate, 3-nitropropionic acid, 2-thenoyltrifluoroacetone, heptyl-hydroxy-quinoline-*N*-oxide, carboxin and oxycarboxin. Crystals were also obtained with 1,2-dinitrobenzene, but only diffracted to 3.0 Å.

2.2.3. Cryoprotection. Although this is still being optimized, a suitable cryoprotectant can be made by mixing one volume of the precipitant with 2/3 volume of 50% glycerol. The crystal is transferred for a few seconds each to a 50:50 mixture of the mother liquor with this cryoprotectant, then to the cryoprotectant alone, followed by immediate freezing in liquid nitrogen. This prevents ice formation and results in useable diffraction, with mosaicity sometimes as low as 0.4°.

2.3. Data collection and processing

Diffraction data were collected at various protein crystallography beamlines at the ALS and SSRL. Data were processed using *DENZO* and reduced with *SCALEPACK* (Otwinowski & Minor, 1997). The combination of relatively high mosaicity after freezing, a moderately long cell axis ($c \simeq 290$ Å) and the tendency of the crystals to orient in the loop with the *c* axis perpendicular to the spindle can lead to problems with spot overlap that need to be taken into consideration when attempting to collect and process high-resolution data.

3. Results and discussion

3.1. Purification

Fig. 1 shows SDS–gel electrophoretic analysis of the preparation at the different stages. Cytochrome spectra show that the THESIT extraction is quite selective for complex II relative to the bc_1 complex and cytochrome oxidase (not shown). This is not apparent from the gel, however, as complex II is a minor component and not really visible in lanes 1–3. After the TSK-gel column the two large subunits are clearly visible and become the main proteins present after hydroxyapatite and DEAE-Sepharose chromatography (lane 6). All four subunits are apparent after ammonium sulfate precipitation in lane 7. The last two steps, gel filtration (lane 8) and density-gradient centrifugation (lane 9), have little effect on the gel profile but may be important for removing aggregated and dissociated complexes, further eliminating non-proteinaceous material such as THESIT and lipids and removing minor interfering protein contaminants. Without the ammonium sulfate precipitation step crystallization was less reproducible and when crystals were obtained they were always embedded in a tough surface film which made mounting for data collection difficult.

3.2. Spectral characterization

Fig. 2 shows the visible spectra of the preparation before and after reducing with a trace of solid sodium dithionite. The spectral features are dominated by the heme, with a Soret peak at 411 nm in the oxidized form that sharpens and shifts to 422 nm upon reduction and broad α and β peaks between 500 and 600 nm that sharpen to 560 and 525 nm in the reduced form. The α peak is asymmetric with a slight shoulder on the short-wavelength side, as also reported for the bovine cytochrome. The same sample of complex II was analyzed for heme by the pyridine hemochrome method (Berry & Trumpower, 1987) and the results were used to put the absorption on an extinction-coefficient scale and to provide approximate heme-based extinction coefficients for the native protein: 16.8 mM^{-1} at 560 *versus* 542 nm for the dithionite-reduced protein and 20.5 mM^{-1} at the same wavelength pair for the reduced-minus-oxidized difference spectrum. These values include the changes arising from absorption by flavin and the iron–sulfur clusters, which we must assume to be present at constant stoichiometry if we use these extinction coefficients to quantitate the complex. These components absorb more in the oxidized than reduced form over most of the visible spectrum and are responsible for the overall decrease in absorption that results in a negative difference absorbance even at the β peak of the cytochrome (Fig. 2).

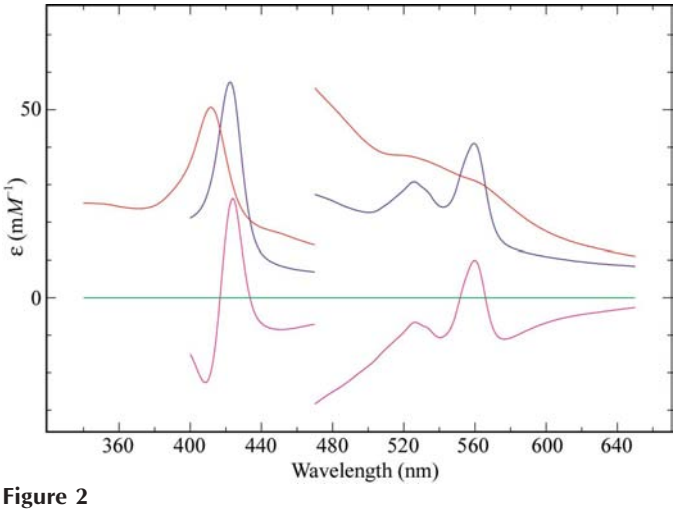

Figure 2
Absorption spectra of the purified avian complex II preparation. Complex II was diluted to 6.8 μ*M* in buffer containing 20 m*M* K-MOPS pH 7.5, 100 m*M* NaCl, 0.5 m*M* EDTA, 0.1 g l^{-1} dodecyl maltoside. A portion of this dilution was used to determine the heme content from pyridine hemechrome spectra as described. Another portion was used directly to take spectra before (red) and after (black) reduction by a trace of solid dithionite. The difference (reduced minus oxidized) is plotted in magenta. The absorption scale has been normalized to directly read the extinction coefficient for the portion of the spectra beyond 470 nm. The region before 470 nm is plotted on a 4× reduced scale.

3.3. Aggregation state

The isolated complex was co-chromatographed with molecular-weight standards on a gel-filtration column (Sephacryl S-300) in the detergent dodecyl maltoside. Complex II eluted slightly behind (*i.e.* at a smaller molecular weight than) the dimeric cytochrome bc_1 complex of *Rhodobacter capsulatus*, which is a 196 kDa protein. This leads us to believe the complex as isolated is monomeric. Blue native-gel electrophoresis, a sensitive technique for the detection of aggregation between respiratory complexes, shows bovine complex II to be monomeric under conditions where other respiratory proteins form supercomplexes (Stroh *et al.*, 2004). The crystal packing in two different cells described below also gives no indication of a physiological multimer. This is in contrast to the *E. coli* complex II protein, which crystallizes as a trimer that is believed to represent the functional state of the protein in the membrane (Yankovskaya *et al.*, 2003).

3.4. Crystallization

When purified and crystallized as described, diffraction-quality crystals are obtained with good reproducibility. The most common form of crystals is in the space group $P2_12_12_1$, with approximate unit-cell parameters $a = 70$, $b = 84$, $c = 290$ Å. On a few occasions using slightly different conditions a second form has been obtained with space group $P2_1$ and unit-cell parameters $a = 120$, $b = 201$, $c = 68$ Å, $\alpha = \beta = \gamma = 90^\circ$.

The $P2_12_12_1$ crystals appear as flat plates which are often rounded in outline, making them appear discoidal. Fig. 3(*a*) shows two such disks in focus, one lying flat and the other viewed edge-on. The crystals in Fig. 3(*b*) have somewhat sharper edges: the crystals are actually improper hexagonal plates that become disk-like when the corner edges are rounded. The *b* and *c* axes are in the plane of the disk, with *a* corresponding to the short dimension or thickness of the disk. A ridge or crease is often visible along the middle of the disk surface (Fig. 2*a*); this is parallel to the *b* axis.

Figs. 3(*a*) and 3(*b*) show small well shaped crystals growing at the rim of the sitting-drop wells one week after setup. Figs. 3(*c*) and 3(*d*) show a larger crystal fished from the depths of its well one month after setup, which is more typical of the crystals used for data collection. It is also a flat plate, viewed face-on in Fig. 3(*c*) and edge-on in Fig. 3(*d*). The mid-face ridge seen in Fig. 3(*c*) is about 20° from the spindle axis, implying that the long *c* axis is 70° from the spindle. The small green circle in Figs. 3(*c*) and 3(*d*) indicates the approximate diameter of the collimated beam (100 µm). With crystals of this size it is possible to collect several data sets from one crystal, with translation between data collections to expose fresh protein each time.

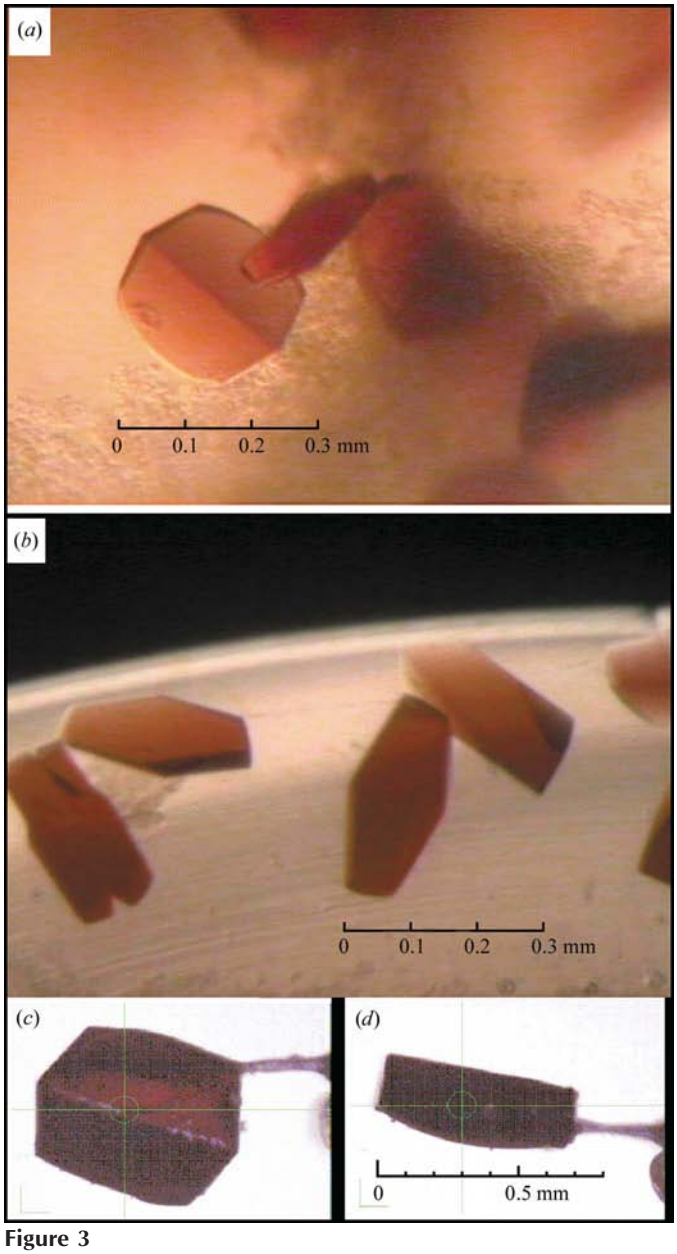

Figure 3
Typical crystals of avian complex II. (*a*) and (*b*) show crystals in two different wells. (*c*) and (*d*) each show a crystal mounted in a nylon loop on the goniometer at beamline 5.0.2 at the ALS. See text for description.

Table 1
Data-reduction statistics for complex II crystal.

The data were collected at SSRL beamline 9-1 on 24 July 2004 using the ADSC Quantum 315 detector (imaging surface 315 × 315 mm). A total of 180° of data were collected in 0.25° oscillations. The crystal-to-detector distance was 400 mm and the exposure time was 10 s normalized for beam intensity. This particular crystal was from co-crystallization with excess oxaloacetate. A table of $I/\sigma(I)$ and R_{sym} *versus* resolution is included in supplementary material for this paper. Values in parentheses are for the highest resolution shell.

Unit-cell parameters (Å)	a = 70.01, b = 84.40, c = 289.50
Solvent content (%)	64
Matthews coefficient V_M (Å^3 Da^{-1})	3.47
X-ray wavelength (Å)	0.979462
Unique reflections	78496
Optical resolution† (Å)	1.76
Wilson B factor (Å^2)	41.0
Mosaicity (°)	0.60
Resolution range (Å)	37.2–2.2 (2.27–2.19)
Completeness (%)	86.6 (48)
Data redundancy	4.4 (1.9)
R_{sym} on I	0.116 (0.270)
$\langle I/\sigma(I)\rangle$	11.8 (2.80)

† Optical resolution: the smallest separation at which features are resolvable, calculated from native Patterson origin peak width by the *SFCHECK* program (Vaguine *et al.*, 1999).

Fig. 4 shows a diffraction pattern from a similar crystal, in this case with the *c* axis about 45° from the spindle. This is a 1° oscillation with the *b***c** plane nearly perpendicular to the beam and *c** running from lower left to upper right. Diffraction is somewhat anisotropic, extending to highest resolution along the *c** axis. Some weak diffraction can be seen in that direction beyond 2.0 Å, as shown in the upper inset of Fig. 4. Preliminary refinement of the structure using *CNS* (Brünger *et al.*, 1998) gives *B*-tensor diagonal elements of +4, +16 and −20.

While we have selected one of the best images from one of the best crystals here, there is not a great deal of variability and most of the variability we observe probably results from poor reproducibility of the cryoprotection and freezing protocol rather than actual differences in the crystals. The data for Table 1 is from a crystal frozen 20 d after setup and the diffraction in Fig. 4 is from a crystal frozen 30 d after setup. With care to keep the wells sealed between data-collection trips, the crystals seem to be stable for at least four months.

3.5. Data collection and processing

Table 1 lists some statistics for data reduction of one of our best data sets. The conditions used and results obtained will be further discussed below. A second table giving R_{sym} and $I/\sigma(I)$ as a function of resolution is available as supplementary material for this paper[1]. The overall resolution is limited by the detector geometry used, which records reflections only to 2.6 Å on the sides of the square and 2.0 Å in the corners. The poor completeness in the last shell, while R_{sym} and $I/\sigma(I)$ still suggest useable data quality, arises from this geometry.

Completeness is 100% in the shell 4.1–3.74 Å and 97.6% for 99–2.6 Å.

The conditions used for collecting the diffraction pattern of Fig. 4 were chosen to demonstrate the resolution limit and are not appropriate for data collection. The closely spaced spots along the c^* axis, which are barely resolved in the image shown, would become closer as that axis rotates out of the plane tangent to Ewald's sphere, leading to severe overlap at a Φ angle 90° from that of the image shown. This problem is usually even more serious: the crystals tend to orient in the oval-shaped loops with their longest dimension along the spindle axis. The longest dimension of the crystal corresponds to the *b* axis, so this puts the *c* axis perpendicular to the spindle axis and thus nearly parallel to the X-ray beam for some range of Φ angles. Together with the sometimes high mosaicity obtained with our current freezing protocol, this makes spot overlap a potential problem that should be taken into account by the data-collection strategy.

Spot overlap can be minimized by optimizing freezing conditions to minimize mosaicity, mounting the crystals properly for data collection about the *c* axis, using longer crystal-to-detector distances, optimizing beamline parameters to minimize spot size and, as a last resort, by special measures during data processing.

Collecting data around the *c* axis is especially effective for this crystal because the other two axes are quite modest in size. Unfortunately, conventional goniometer arcs and κ-jigs are not practical at the end-stations we use owing to close tolerances required to avoid collisions with other parts of the camera. The tendency of the crystals to align the *b* axis with the spindle can be overcome by picking up the crystal spatula-wise using a smaller loop, paying attention that the crease on the face of the crystal is perpendicular to the pin. Newly available microfabricated crystal mounts (Thorne *et al.*, 2003) may be useful here, providing a round hole of accurate size, a flat surface surrounding the hole and rigidity to prevent bending under the weight of the crystal.

In the case of the data collection described in Table 1 the *c* axis was nearly perpendicular (80°) to the spindle axis; however, the mosaicity was unusually low (0.596°; from post-refinement of data processed assuming 0.7°) and by reintegrating with an assumed mosaicity of 0.5° we were able to achieve the indicated completeness, limited mainly by the edges of the detector, with no significant increase in $R_{\rm sym}$. The actual $R_{\rm sym}$ values are surprisingly high even in the low-resolution shells (0.096 for 99–4.71 Å); however, this is not a consequence of integrating with underestimated mosaicity, as similar $R_{\rm merge}$ values were obtained assuming a mosaicity of 0.7° or even 1.5°. It also does not arise from anomalous scattering from the abundant iron in this protein, as scaling Bijvoet mates separately did not decrease the χ^2 values. It probably results from overlap of intensity from one spot into the next spot's profile.

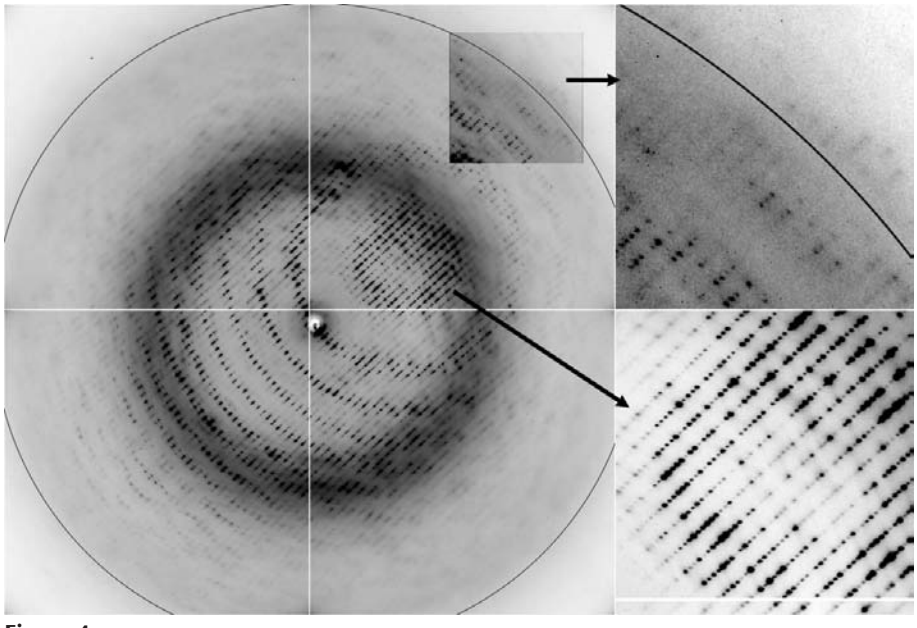

Figure 4
A diffraction pattern of orthorhombic chicken mitochondrial complex II: a 1.0° oscillation diffraction pattern from one of the better complex II crystals at ALS beamline 5.0.1, with exposure 120 s and distance 200 mm, recorded on the ADSC Quantum 210 detector. The entire detector surface (210 × 210 mm) is shown in the main picture. A circle is drawn at a resolution of 2.00 Å. A small square area around 2.0 Å in the upper right quadrant is shown with increased contrast and part of that area is enlarged 3× in the upper right inset. Another region in the low-resolution area is shown magnified 3× and with reduced contrast in the lower right inset. The crystal is mounted so that the *c* axis is about 45° from the spindle axis and rotated about the spindle axis until the *c* axis is nearly perpendicular to the beam for this exposure. The concentric lunes are made up of reflections with constant values of *h*, while *k* varies from upper left to lower right and *l* from lower left to upper right (diagonal lines of barely resolved spots).

3.6. Phasing and model building

The crystals were solved by molecular replacement using the structure of the *E. coli* SDH complex (PDB code 1nek) as a search model. After we succeeded in lowering the *R* factor below 0.40 by manual rebuilding in the poorly phased density maps, the *ARP*/*wARP* procedure (Perrakis *et al.*, 2001) was able to improve phases and build most of the model, as well as providing excellent maps for building the difficult parts. At present all but 23 residues out of 1117 have been built and the model is being refined against 2.2 Å data with a current $R_{\rm free}$ and *R* of 0.24 and 0.21, respectively. There is density at the substrate and quinone sites consistent with oxaloacetate and ubiquinone, although other occupants cannot be ruled out at this resolution and stage of refinement. Oxaloacetate may be covalently bound. Strands of density presumably corresponding to phospholipids and perhaps the polyprenyl side chain of ubiquinone are present in the membrane domain.

3.7. Crystal packing

There is one monomer (heterotetramer) in the asymmetric unit of the $P2_12_12_1$ crystal, giving a Matthews coefficient of 3.47 Å^3 Da^{-1} and a solvent content of about 64%. The packing is illustrated in Fig. 5 and shows that the crystals are of Michel's 'type I' (Deisenhofer & Michel, 1989): the transmembrane helical regions form bands suggestive of membrane layers in a stack of two-dimensional crystals, with the membrane layers perpendicular to the *c* axis. The twofold screw axes along *a* and *b* are within the plane of the membrane and relate adjacent monomers with alternate up/down orientation in the membrane. The screw axis along *c* relates adjacent membrane layers. Protein in the membrane layer is quite tightly packed and although only half the extrinsic domains go to each side of the membrane, because the extrinsic domains are wider than the membrane domains these layers are also well packed. As a result, the extrinsic domains from adjacent membrane layers do not interdigitate but stack in such a way that each pair of adjacent membrane layers is separated by two layers of extrinsic domains. Moving up along the *c* axis, one passes through a membrane layer, then a layer of extrinsic domains of upwardly oriented molecules from that membrane, then a layer of extrinsic domains from downwardly oriented molecules in the next membrane and then the next membrane. The repeating unit consists of two membrane layers and four extrinsic layers, resulting in the long *c* axis of 291 Å.

The packing has also been determined for the $P2_1$ cell and is shown in Fig. 5(*b*). There is a dimer in the asymmetric unit and here also the membrane and extrinsic domains of the protein molecules line up in bands perpendicular to the long axis (*b* in this case), suggesting stacks of two-dimensional crystals. The noncrystallographic symmetry is almost a proper twofold axis in the membrane plane and relates an up–down pair of adjacent molecules, which pack their membrane domains closely together (cyan and red molecules in Fig. 5*b*). Otherwise, packing in the membrane is rather loose (note the gap between the membrane domains of the red and brown molecules). In this case, the extrinsic domains from adjacent membranes interdigitate, with the extrinsic domains of downwardly oriented molecules from the membrane above alternating with upwardly oriented molecules from the membrane below. Dense packing in the extrinsic layers makes up for loose packing in the membrane and V_M is slightly smaller for this form than for the first form. As a result of the

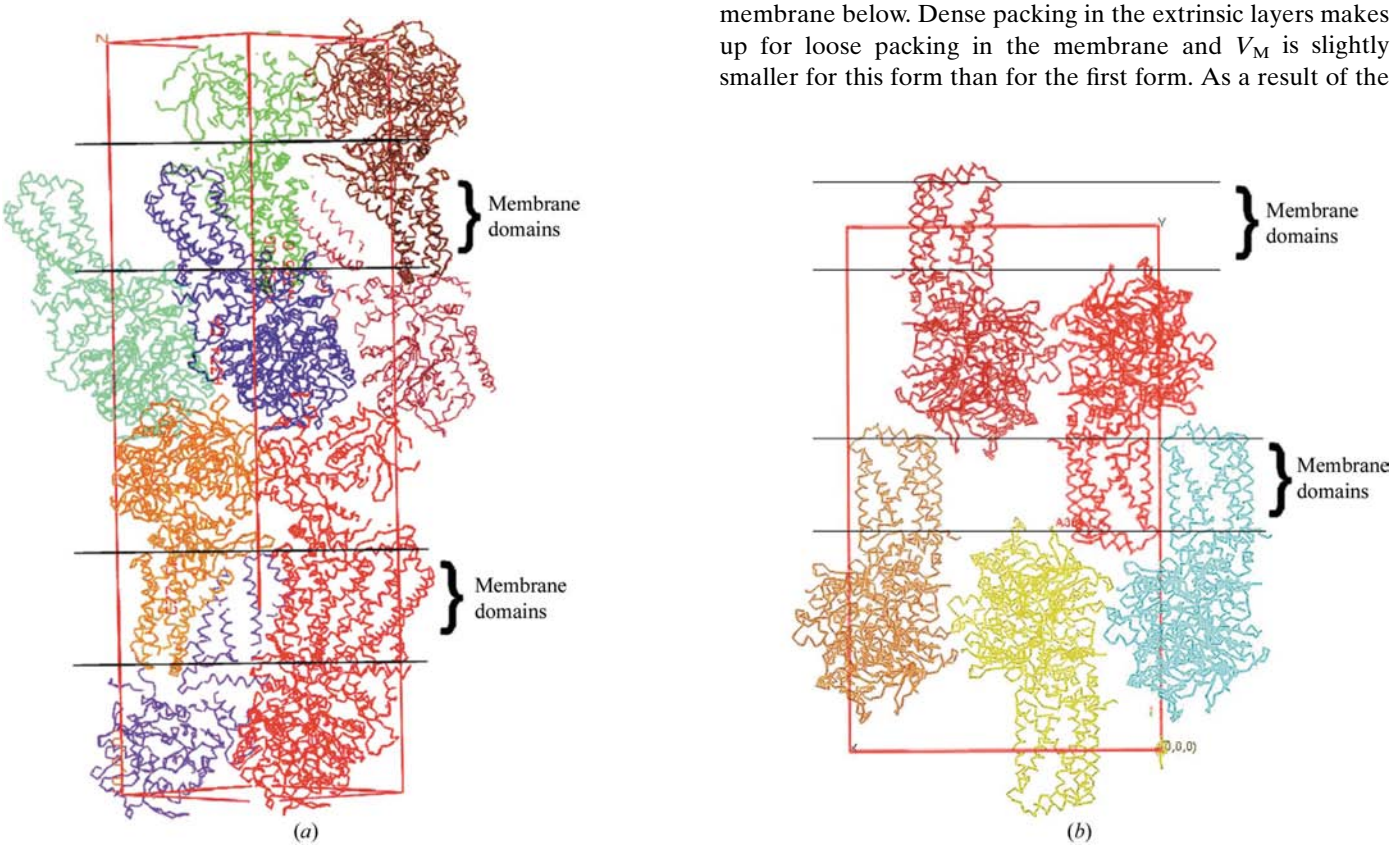

Figure 5
Crystal packing in the orthorhombic complex II crystals reveal them to be 'type 1' crystals. In both crystal forms the cell contains four molecules. The crystal contains zones parallel to the *ab* plane consisting of transmembrane helix regions, suggesting that the crystals are stacks of two-dimensional membrane crystals as described by Michel (his 'type 1' crystals). Each such membranous zone has complex II molecules inserted alternately from opposite sides. (*a*) $P2_12_12_1$ crystals: the unit cell spans two such membranes related by the twofold screw axis along *c* (perpendicular to the membrane). Adjacent molecules within each membrane are related by the screw axes along *a* and *b*, as is often observed in two-dimensional crystals of membrane proteins. Between adjacent membrane zones are two zones of extrinsic domains, one from each membrane, resulting in the long *c* axis of this crystal form. (*b*) $P2_1$ crystals. The unit cell spans two membranes related by the twofold screw axis along *b*. The pseudo-twofold axis about *c* is within the membrane plane, relating adjacent up- and down-oriented molecules such as the red and blue molecules depicted. Extrinsic domains from two adjacent membranes interdigitate, allowing the membranes to stack more closely and resulting in the shorter longest axis of this crystal form. Along the *c* axis (perpendicular to the plane of the picture) there is only translational symmetry; that is, more molecules exactly behind those depicted.

interdigitation, there is only one layer of extrinsic domains between each pair of adjacent membranes and the long axis, which is again perpendicular to the membrane plane and includes two membranes related by a twofold screw axis, is shortened by about 90 Å to 201 Å. The noncrystallographic axis is perpendicular to the screw axis and results in pseudo-symmetry of $P2_12_12$ (and $\beta \simeq 90^\circ$). The NCS is a twofold rotation about an axis parallel to *c* but with a screw component of ∼3 Å per 180° rotation. The long axis of only 201 Å should facilitate data collection if this form can be routinely made to diffract to high resolution. In addition, the different crystal contacts in the two crystals will help elucidate the effects of crystal contacts on the intrinsic structure in both forms and if there are disordered regions in one form they may be clear in the other.

4. Conclusions

A procedure is presented for preparation of diffraction-quality crystals of a vertebrate mitochondrial respiratory complex II. The crystals have the potential to diffract to at least 2.0 Å with optimization of post-crystal-growth treatment and cryoprotection. This should allow determination of the structure of this important and medically relevant membrane-protein complex at near-atomic resolution and provide great detail of the mode of binding of substrates and inhibitors at the two substrate-binding sites.

This work was supported by NIH grants GM62563 (NIGMS) and DK44842 (NIDDK). Lawrence Berkeley National Laboratory is operated by the Department of Energy, contract DE-AC03-76SF00098 to the University of California. Diffraction data were collected at the Advanced Light Source (ALS) at LBNL and at the Stanford Synchrotron Radiation Laboratory (SSRL), which is operated by the Department of Energy, Office of Basic Energy Sciences. The SSRL Biotechnology Program is supported by the National Institutes of Health, National Center for Research Resources, Biomedical Technology Program and by the Department of Energy, Office of Biological and Environmental Research. We would like to thank Tzanko Doukov and Paul Ellis at SSRL and Corie Ralston, Christine Trame, Jeff Dickert and Azer Dauz at the ALS for help with data collection, and Ning G. Pon for critically reading the manuscript.

References

Ackrell, B. A. (2000). *FEBS Lett.* **466**, 1–5.
Ackrell, B. A. (2002). *Mol. Aspects Med.* **23**, 369–384.
Albayrak, T., Scherhammer, V., Schoenfeld, N., Braziulis, E., Mund, T., Bauer, M. K., Scheffler, I. E. & Grimm, S. (2003). *Mol. Biol. Cell*, **14**, 3082–3096.
Baysal, B. E., Ferrell, R. E., Willett-Brozick, J. E., Lawrence, E. C., Myssiorek, D., Bosch, A., van der Mey, A., Taschner, P. E., Rubinstein, W. S., Myers, E. N., Richard, C. W. III, Cornelisse, C. J., Devilee, P. & Devlin, B. (2000). *Science*, **287**, 848–851.
Beal, M. F., Brouillet, E., Jenkins, B. G., Ferrante, R. J., Kowall, N. W., Miller, J. M., Storey, E., Srivastava, R., Rosen, B. R. & Hyman, B. T. (1993). *J. Neurosci.* **13**, 4181–4192.
Bernath, P., Kearney, E. B. & Singer, T. P. (1956). *J. Biol. Chem.* **223**, 599–613.
Berry, E. A. & Trumpower, B. L. (1987). *Anal. Biochem.* **161**, 1–15.
Boardman, P. E., Sanz-Ezquerro, J., Overton, I., Burt, D., Bosch, E., Fong, W., Tickle, C., Brown, W., Wilson, S. & Hubbard, S. (2002). *Curr. Biol.* **12**, 1965–1969.
Brünger, A. T., Adams, P. D., Clore, G. M., DeLano, W. L., Gros, P., Grosse-Kunstleve, R. W., Jiang, J.-S., Kuszewski, J., Nilges, M., Pannu, N. S., Read, R. J., Rice, L. M., Simonson, T. & Warren, G. L. (1998). *Acta Cryst.* D**54**, 905–921.
Cecchini, G. (2003). *Annu. Rev. Biochem.* **72**, 77–109.
Cecchini, G., Schroder, I., Gunsalus, R. P. & Maklashina, E. (2002). *Biochim. Biophys. Acta*, **1553**, 140–157.
Davis, K. A. & Hatefi, Y. (1971*a*). *Biochem. Biophys. Res. Commun.* **44**, 1338–1344.
Davis, K. A. & Hatefi, Y. (1971*b*). *Biochemistry*, **10**, 2509–2516.
Deisenhofer, J. & Michel, H. (1989). *EMBO J.* **8**, 2149–2170.
Green, D. E., Wharton, D. C., Tsagoloff, A., Rieske, J. S. & Brierley, G. P. (1965). *Oxidase and Related Redox Systems*, edited by T. E. King, H. S. Mason & M. Morrison, pp. 1032–1076. New York: John Wiley.
Hagerhall, C. (1997). *Biochim. Biophys. Acta*, **1320**, 107–141.
Ito, Y., Muraguchi, H., Seshime, Y., Oita, S. & Yanagi, S. O. (2004). *Mol. Genet. Genomics*, **272**, 328–335.
Iverson, T. M., Luna-Chavez, C., Croal, L. R., Cecchini, G. & Rees, D. C. (2002). *J. Biol. Chem.* **277**, 16124–16130.
Lancaster, C. R. (2001). *FEBS Lett.* **504**, 133–141.
Lancaster, C. R. (2003). *FEBS Lett.* **555**, 21–28.
McDonnell, C. M., Benn, D. E., Marsh, D. J., Robinson, B. G. & Zacharin, M. R. (2004). *Clin. Endocrinol. (Oxf)*, **61**, 510–514.
Niemann, S. & Muller, U. (2000). *Nature Genet.* **26**, 268–270.
Otwinowski, Z. & Minor, W. (1997). *Methods Enzymol.* **276**, 307–326.
Oyedotun, K. S. & Lemire, B. D. (2004). *J. Biol. Chem.* **279**, 9424–9431.
Perrakis, A., Harkiolaki, M., Wilson, K. S. & Lamzin, V. S. (2001). *Acta Cryst.* D**57**, 1445–1450.
Singer, T. P., Kearney, E. B. & Kenney, W. C. (1973). *Adv. Enzymol. Relat. Areas Mol. Biol.* **37**, 189–272.
Smith, A. L. (1967). *Methods Enzymol.* **10**, 81–86.
Stroh, A., Anderka, O., Pfeiffer, K., Yagi, T., Finel, M., Ludwig, B. & Schagger, H. (2004). *J. Biol. Chem.* **279**, 5000–5007.
Thorne, R. E., Stum, Z., Kmetko, J., O'Neill, K. & Gillilan, R. (2003). *J. Appl. Cryst.* **36**, 1455–1460.
Vaguine, A. A., Richelle, J. & Wodak, S. J. (1999). *Acta Cryst.* D**55**, 191–205.
Wang, T. Y., Tsou, C. L. & Wang, Y. L. (1956). *Sci. Sin.* **5**, 1956.
Wikstrom, M. K. (1973). *Biochim. Biophys. Acta*, **301**, 155–193.
Yankovskaya, V., Horsefield, R., Tornroth, S., Luna-Chavez, C., Miyoshi, H., Leger, C., Byrne, B., Cecchini, G. & Iwata, S. (2003). *Science*, **299**, 700–704.
Yu, C. A. & Yu, L. (1980). *Biochim. Biophys. Acta*, **591**, 409–420.